

TiO₂ Nanofibers Decorated with Monodispersed WO₃ Heterostructure Sensors for High Gas Sensing Performance Towards H₂ Gas

M Kumaresan (✉ kumaresan084@gmail.com)

Hindusthan College of Arts and Science <https://orcid.org/0000-0001-6456-9181>

M. Venkatachalam

Erode Arts and Science College

M. Saroja

Erode Arts and Science College

P. Gowthaman

Erode Arts and Science College

Research Article

Keywords: WO₃, TiO₂ nanofibers, Heterojunction, Chemical sensor, Hydrogen gas, High sensitivity

Posted Date: March 13th, 2021

DOI: <https://doi.org/10.21203/rs.3.rs-285097/v1>

License:  This work is licensed under a Creative Commons Attribution 4.0 International License.

[Read Full License](#)

Abstract

A simple spin coating method was used to prepare the $\text{WO}_3\text{-TiO}_2$ heterostructural nanofibers (HNFs). Various kinds of techniques, including XRD, SEM, TEM, EDS and XPS, have described the structures, chemical constitutions and morphologies of the samples. Following the decoration of the WO_3 nanocubes on the surface of TiO_2 nanofibers, XPS findings confirmed the presence of W^{5+} and the excess proportion of both chemisorbed reactive oxygen and oxygen vacancies. WO_3 incorporated TiO_2 thin film sensor showed high sensing response (78%), rapid response (20 s) and recovery time (23 s) with respect to other gas molecules (NH_3 , NO_2 , LPG and SO_2). The finding demonstrates that the $\text{WO}_3\text{-TiO}_2$ sensor showed good selective response towards H_2 gas. A unique path was created by this work to build hetero-highly ordered mesoporous metal oxides junctions for applications in H_2 gas sensor based devices.

1. Introduction

With the need to identify the amount of toxic gases (NO , NO_2 , CO , SO_2 , H_2S , etc.) in the air in real time, the development of high-performance gas sensors in the manufacturing, ecological and health sectors is essential. Due to its benefits such as simple design, long lifetime, compact size and n, the semiconductor gas sensor is one of the most popular consistently applied sensors [1, 2]. The core part of the semiconductor gas sensor as a sensitive coating. A multitude of compounds, such as ZnO [3, 4], SnO_2 [5, 6] and Fe_2O_3 [7, 8], were used to manufacture gas-sensitive coatings. However these frameworks have some drawbacks, such as low response, high energy consumption, and some humidity and temperature volatility. WO_3 has exceptionally high sensitivity for NO_2 detection compared to the conventional materials above [9, 10], and is a suitable candidate for gas sensor coating materials. And it is also stated that the doping into WO_3 of another kind of oxides leads to the formation of semiconductor heterojunction, thereby increasing overall the coatings' gas sensitivity.

TiO_2 is well established to be a kind of semiconductor material with excellent electrical properties. Improvements have been documented in the gas sensitivity of semiconductor WO_3 induced by TiO_2 doping. However, the latest TiO_2 doping methods, which are not suitable for commercial development, are highly complex. In fact, the gas control problem of the TiO_2 -doped coatings has still not been clearly established. The WO_3 -based composite coatings doped with TiO_2 were prepared by liquid-phase plasma spraying in this paper as per that concern, and the gas-sensing process of $\text{TiO}_2\text{-WO}_3$ composite coatings was extensively investigated. As already mentioned, it is also proved to be a potential method is tested loaded on a support material due to its delicate conductivity, strong catalytic properties, and remarkable chemical inertness. Nanofiber $\text{WO}_3\text{-TiO}_2$ may form n-n heterojunction, which can potentially present highly explosive localized areas and thus obtain unpredictable features for specific applications. In this analysis, we describe a simple and successful spin coating technique has been used to fabricated the quasi-1D WO_3 nanoparticles-decorated TiO_2 heterostructural nanofibers. High response, discern

specificity, quick response time and recovery time for H₂ gas were demonstrated by the as-prepared WO₃-TiO₂ material, making it a successful candidate for application in H₂ sensors. A sensor adsorption and reaction model has also been suggested. The increase in the efficiency of gas sensing can be due to the creation of heterojunctions seen between two material types.

2. Experimental Process

2.1. Chemicals and Reagents

Tungsten chloride (WCl₆), Titanium tetra-isopropoxide (TTIP) with a normal purity of 97% (Aldrich, UK), Ammonia solution (NH₄OH), Hydrochloric acid (HCl) was purchased and used as without extra purification.

2.2. Preparation of WO₃/TiO₂ thin films

The process of making WO₃/TiO₂ films involves two step synthesis processes. Hydrothermal and spin coating technique has been used to fabricate the bare WO₃ and TiO₂ thin films, respectively. Firstly, WCl₆ was distributed in 30 mL deionized water through magnetic stirring for 20 min. Later, 5 mL of HCl aqueous solution was added and the reaction mixture was fully dissolved by thoroughly mixing for another 10 min. the reaction mixture was adapted to hydrothermal reaction (180 °C/12 h) and finally dried (80 °C/12 h) for further use. Spin coating method was used to fabricate the TiO₂ nanotubes. FTO substrate was used to deposit the thin films. The raw materials of TiO₂ precursors (5 mL TTIP with 1:1 ratio of ethanol and DI water) was deposited on FTO glass substrate at speed of 2000 rpm for 1 min. The films after drying at 120 °C for 5 min are subsequently heat-treated at 450 °C for 30 min in nitrogen flow. In the process of WO₃/TiO₂ composite. The prepared WO₃ nanopowder (0.5 g) was dispersed in the 0.5 g of TiO₂ nanofibers and same experimental process of spin coating method has been repeated for each concentrations. The films with WO₃ nanoparticles, TiO₂ nanofibers and WO₃/TiO₂ heterostructures were labeled as WO₃ NPs, TiO₂ NFs and WO₃/TiO₂ Hs, respectively.

2.3. Gas sensor set up with sensor region

The gas sensor of the resistive form was constructed and the schematic view is being shown in Fig. 1. The detailed description of the sensor was mentioned already our previous reported work [11]. The mass flow controller (MFC) was used to modify gas concentrations at various ppm levels (0-1000 ppm). The gases were connected to the mass flow controller with a mixer from different cylinder. The diluted gases were then evenly located in the testing reactor. The gas sensing response (S) was stated as $(R_G - R_A) / R_A \times 100\%$ [12], where the air resistance value and the corresponding gas were R_G and R_A, respectively.

3. Results And Discussion

3.1. X-ray diffraction (XRD) analysis

Figure 2 shows the XRD pattern of WO_3 NPs, TiO_2 NFs and WO_3/TiO_2 Hs films respectively. The pattern clearly expose the bare WO_3 and TiO_2 are monoclinic (JCPDS card No. 43-1035) and anatase phase tetragonal rutile type structure (JCPDS card No. 21-1272). Sharp intense peaks without any contaminant suggest that fabricated films are high order crystalline nature. The diffraction peaks of the $\text{WO}_3\text{-TiO}_2$ can be indexed to the mixed WO_3 and TiO_2 with different phases and no apparent peak change relative to the pure materials, which shows that the end product contains of it rather than alloy WO_3 and TiO_2 nanocomposites.

3.2. Morphological studies

The morphological detection of the sensors was examined by SEM and TEM. Figure 2 (a-c) shows the SEM images of WO_3 NPs, TiO_2 NFs and WO_3/TiO_2 Hs films respectively. Monodispersed spherical of WO_3 and tubes like TiO_2 morphologies are recognized by the SEM images. Further the clear morphological view was identified their corresponding TEM images. The TEM image of WO_3 and TiO_2 clearly demonstrate that less aggregated nanoparticles with uniform tube like morphologies were found. In the WO_3/TiO_2 heterostructure composite, the nanoparticles are uniformly grown on the surface of the TiO_2 nanotubes. Without obvious aggregation and combining, the framework of TiO_2 nanofibers is advantageous for getting high surface area and improving the catalytic process of gas sensing. The elemental mapping of WO_3/TiO_2 Hs films shows W, Ti and O elements on the surface of the images (Fig. 3g-i).

3.3. Surface and elemental composition studies

Brunauer–Emmett–Teller (BET) method was used to describe the porous structure and clear surface areas of sensors through their N_2 adsorption-desorption analysis as well as pore size distribution curve (Fig. 4a & b). All the samples display category IV nitrogen isotherm with a hysteresis loop, suggesting the features of mesopores [13–17]. Due to the heterostructure combination of WO_3 nanoparticles and TiO_2 nanofibers can deliver the high surface area ($104.7 \text{ m}^2/\text{g}$) and pore size (17.4 nm) than that of bare WO_3 ($54.3 \text{ m}^2/\text{g}$ and 37.4 nm) and TiO_2 ($77 \text{ m}^2/\text{g}$ and 30.2 nm). The chemical state and composition of elemental configuration was analyzed by XPS. The survey XPS of WO_3/TiO_2 Hs shows the chief elements of W, Ti and O (Fig. 5a). Figure 5 (b-d) displays the high resolution spectrum of the W 4f, Ti 2p and O 1s spectra. The divided peaks based at the binding energies of 34.9 and 36.8 eV correspond to the standard binding energies of W^{5+} [18, 19] in the W 4f XPS spectrum. With binding energies at 465.2 eV and 459.6 eV, the Ti 2p XPS spectrum can be deconvoluted into two major peaks, corresponding to Ti $2\text{p}_{1/2}$ and Ti $2\text{p}_{3/2}$. The distinctiveness peaks of O_2^- and O^- are located with equivalent binding energies of 530.4 eV and 531.5 eV, respectively [20, 21].

3.5. Gas sensing test

The efficiency of the gas sensing performance of the H_2 gas was tested by using the WO_3 , TiO_2 and WO_3/TiO_2 sensor materials. Before gas sensing test the sensor samples were exposed to air atmosphere

to identify the resistivity performance of the samples and the relevant graph illustrates that good resistive nature for all the sensor samples (Fig. 6a). The sensing response is shown in Fig. 6 (b). The dynamic response is drastically enhanced with the increase of H₂ gas concentration from 0 to 1000 ppm (Fig. 6c). The maximum sensitivity is achieved by WO₃/TiO₂ Hs (78%) than compared with bare WO₃ (27%) and TiO₂ (52%) sensor films. In addition, the impact of the degree of doping on the ordered quality of the porous channel and relative humidity (RH) on sensing characteristics was also investigated and the relevant plot is shown in Fig. 7 (a). The analysis indicates that the sensor based on WO₃/TiO₂ Hs offered the highest response, regardless of the test conditions. The high performance of the WO₃/TiO₂ Hs based sensor ought to be beneficial for the unique and powerful structure effect and doping effect because the mesoporous structure could provide both high surface area and prosperous for hydrogen gas adsorption and diffusion (structure effect) while doping means improving defects and active site. For industrial cases, the reaction and recovery time of gas sensors is quite important. The H₂ gas concentration I exposed to 1000 ppm at RT towards all the sensor films and the finding reveals that WO₃/TiO₂ Hs sensors gained rapid response (20s) and recovery time (23 s) than other sensors (Fig. 7b-d). The H₂ gas parameters of all the sensors are estimated and the values are displayed in Table 1. Finally, we carried out a response comparison of the sensors 1000 ppm of different target gases to affirm the progress in selectivity. Figure 8 (a-c) selectivity characteristics graph of all the sensors, which is exposed to various target gases like, NH₃, NO₂, LPG and SO₂. The sensor stability is often continually monitored. As shown in Fig. 8d, the curve showed a remarkably stable tendency toward 1000 ppm H₂ gas throughout a 60-day long-term stability calculation. In addition, no noticeable decline in response pattern is found for detecting 1000 ppm H₂ gas after 50 successive tests (Fig. 8d). These findings show that the HNFs-based WO₃/TiO₂ sensor has strong reproducibility and long-term reliability. The sensing mechanism with graphical sketch of the proposed sensor is shown in Fig. 9. The improved sensing performance of the HNFs-based WO₃/TiO₂ sensor is due to the following reasons: On the one side, the Fermi level of WO₃ is lower for WO₃/TiO₂ HNFs than for TiO₂, which contributes to the transport of energy from TiO₂ to WO₃ till the level of Fermi energy is equivalent. As a consequence, on the side of WO₃, the electron diffusion surface will develop, that will make it much easier to accumulate oxygen or target gasses on the WO₃. Consequently, WO₃ nanospheres serve as a responsive active site on the surface of TiO₂ nanotubes and have a beneficial effect on H₂ sensor output. It clearly suggests that the gas sensing efficiency of this sensor is obviously advantageous over that of other sensors.

4. Conclusions

In this report, the WO₃ nanoparticles incorporated TiO₂ heterostructures with mesoporous nature films sensors were fabricated and tested the gas sensing response towards H₂ gas with at RT. The heterostructure which facilitated the fabrication of a sensitive and porous shaped sensing film. WO₃/TiO₂ heterostructure thin film sensor showed high sensing response (78%), rapid response (20 s) and recovery time (23 s) with respect to other gas molecules (NH₃, NO₂, LPG and SO₂). In addition that the fabricated sensors also exhibit long term stability due no apparent loss in sensitivity after multiple cycle

experiments. The finding demonstrates that the $\text{WO}_3\text{-TiO}_2$ sensor showed good selective response towards H_2 gas. The $\text{WO}_3\text{-TiO}_2$ HNFs sensor's excellent performance could be related to the existence of n-n junctions as well as the redox of W^{6+} and W^{5+} states. The results confirmed that the significant insight $\text{WO}_3\text{-TiO}_2$ HNFs was a good approach for a high-performance H_2 sensor.

References

1. Franke ME, Koplín TJ, Simon U. Metal and metal oxides nanoparticles in chemiresistors: does the nanoscale matter? *Small*. 2 (2006) 36–50.
2. Tricoli A, Righettoni M, Teleki A. Semiconductor gas sensors: dry synthesis and application. *Angew Chem Int Ed*. 49 (2010) 7632–7659.
3. Wan Q, Li QH, Chen YJ, Wang TH, He XL, Li JP, et al. Fabrication and ethanol sensing characteristics of ZnO nanowire gas sensors. *Appl. Phys. Lett.* 84 (2004) 3654–3656.
4. Zhang J, Wang S, Wang Y, Xu M, Xia H, Zhang S, et al. ZnO hollow spheres: preparation, characterization, and gas sensing properties. *Sens Actuators B: Chem.* 139 (2009) 411–417.
5. Wei F, Zhang H, Nguyen M, Ying M, Gao R, Jiao Z. Template-free synthesis of flower-like SnO_2 hierarchical nanostructures with improved gas sensing performance. *Sens Actuators B: Chem.* 215 (2015) 15–23.
6. Sun P, Cao Y, Liu J, Sun Y, Ma J, Lu G. Dispersive SnO_2 nanosheets: hydrothermal synthesis and gas sensing properties. *Sens. Actuators B: Chem.* 156 (2011) 779–783.
7. Chen J, Xu LN, Li WY, Gou XG. $\alpha\text{-Fe}_2\text{O}_3$ nanotubes in gas sensor and lithium-ion battery applications. *Adv. Mater.* 17 (2005) 582–586.
8. Ouyang J, Pei J, Kuang Q, Xie Z, Zheng L. Supersaturation-controlled shape evolution of $\alpha\text{-Fe}_2\text{O}_3$ nanocrystals and their facet-dependent catalytic and sensing properties. *ACS Appl. Mater. Interfaces*. 6 (2014) 12505–12514.
9. Espid E, Taghipour F. Development of highly sensitive $\text{ZnO}/\text{In}_2\text{O}_3$ composite gas sensor activated by UV-LED. *Sens Actuators B*. 241 (2016) 828–839.
10. Baranov A, Spirjakín D, Akbari S, Somov A. Optimization of power consumption for gas sensor nodes: a survey. *Sens. Actuators A*. 233 (2015) 279–289.
11. K.H. Kim, M. Yang, K.M. Cho, Y.S. Jun, S.B. Lee, H.T. Jung, High quality reduced graphene oxide through repairing with multi-layered graphene ball nanostructures, *Nat. Sci. Rep.* 3 (2013) 3251–3258.
12. S. Ryabtsev, A. Shaposhnik, A. Lukin, E. Domashevskaya, *Sensors and Actuators B: Chemical*. 59 (1999) 26.
13. M. Sumathi, A. Prakasam, P.M. Anbarasan, High capable visible light driven photocatalytic activity of $\text{WO}_3/\text{g-C}_3\text{N}_4$ heterostructure catalysts synthesized by a novel one step microwave irradiation route, *J. Mater. Sci. Mater. Electron.* 30 (2019) 3294–3304.

14. M. Sumathi, A. Prakasam, P.M. Anbarasan, Fabrication of hexagonal disc shaped nanoparticles g- C_3N_4 /NiO heterostructured nanocomposites for efficient visible light photocatalytic performance, *Journal of Cluster Science* 30 (2019) 757–766.
15. M. Parthibavarman, S. Sathishkumar, M. Jayashree, R. BoopathiRaja, [Microwave Assisted Synthesis of Pure and Ag Doped \$SnO_2\$ Quantum Dots as Novel Platform for High Photocatalytic Activity Performance](#), *Journal of Cluster Science* 30 (2019) 351-363
16. M. Parthibavarman, S. Sathishkumar, S. Prabhakaran, M. Jayashree, R. BoopathiRaja, [High visible light-driven photocatalytic activity of large surface area Cu doped \$SnO_2\$ nanorods synthesized by novel one-step microwave irradiation method](#), *Journal of the Iranian Chemical Society* 15 (2018) 2789-2801
17. R. BoopathiRaja, M. Parthibavarman, [Hetero-structure arrays of \$MnCo_2O_4\$ nanoflakes@ nanowires grown on Ni foam: Design, fabrication and applications in electrochemical energy storage](#), *J. Alloy. Compd.* 811 (2019) 152084
18. N. Feng, Q. Wang, A. Zheng, Z. Zhang, J. Fan, S.B. Liu, et al., Understanding the high photocatalytic activity of (B, Ag)-codoped TiO_2 under solar-light irradiation with XPS, solid-state NMR, and DFT calculations, *J. Am. Chem. Soc.* 135 (4) (2013) 1607–1616,
19. Y. Zhang, J. Chen, L. Hua, S. Li, X. Zhang, W. Sheng, et al., High photocatalytic activity of hierarchical SiO_2 @C-doped TiO_2 hollow spheres in UV and visible light towards degradation of of rhodamine B, *J. Hazard. Mater.* 15 (2017) 309-318
20. J.-C. Dupin, D. Gonbeau, P. Vinatier, A. Levasseur, Systematic XPS studies of metal oxides, hydroxides and peroxides, *Phys. Chem. Chem. Phys.* 2 (2000) 1319–1324.
21. R. Sivakumar, R. Gopalakrishnan, M. Jayachandran, C. Sanjeeviraja, Investigation of X-ray photoelectron spectroscopic (XPS), cyclic voltammetric analyses of WO_3 films and their electrochromic response in FTO/ WO_3 /electrolyte/FTO cells, *Smart Mater. Struct.* 15 (2006) 877–888

Table

Due to technical limitations, table 1 is only available as a download in the Supplemental Files section.

Figures

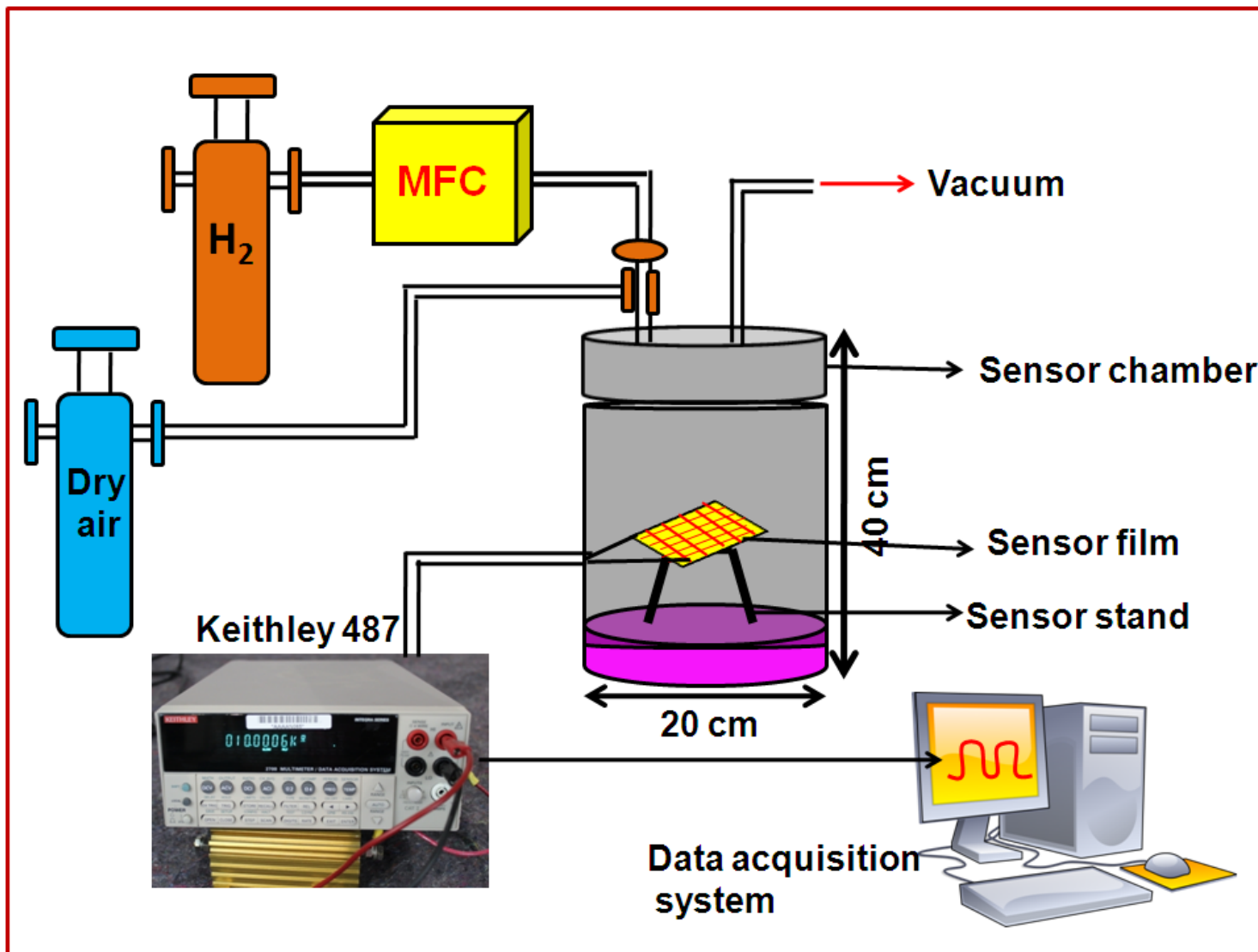


Figure 1

Schematic representation of the gas sensor setup

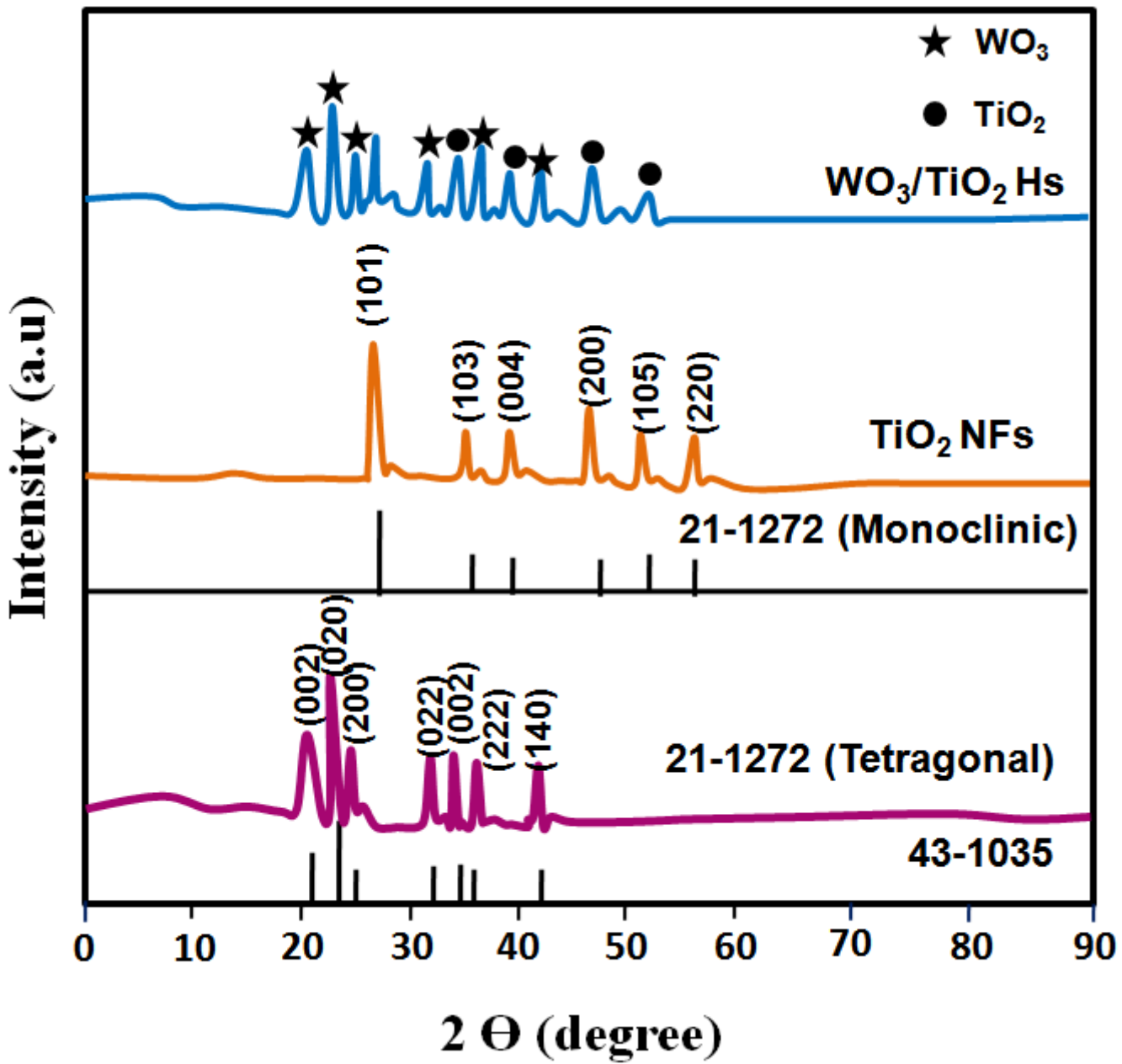


Figure 2

X-ray diffraction pattern of the sensor films

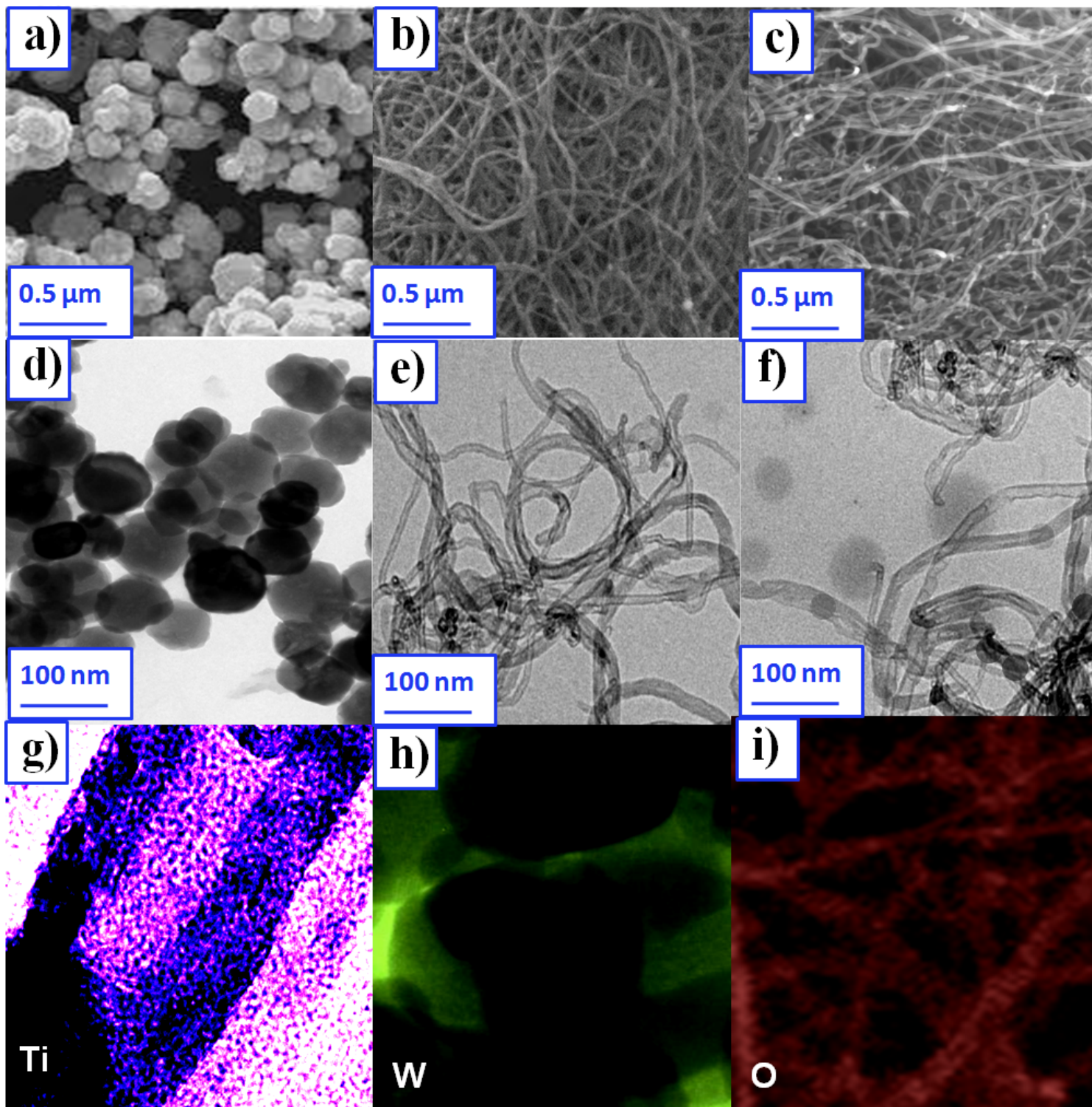


Figure 3

SEM images of (a) WO₃ NPs; (b) TiO₂ NFs; (c) WO₃/TiO₂ Hs; TEM images of (d) WO₃ NPs; (e) TiO₂ NFs; (f) WO₃/TiO₂ Hs; Elemental mapping of (g) Ti; (h) W and (i) O

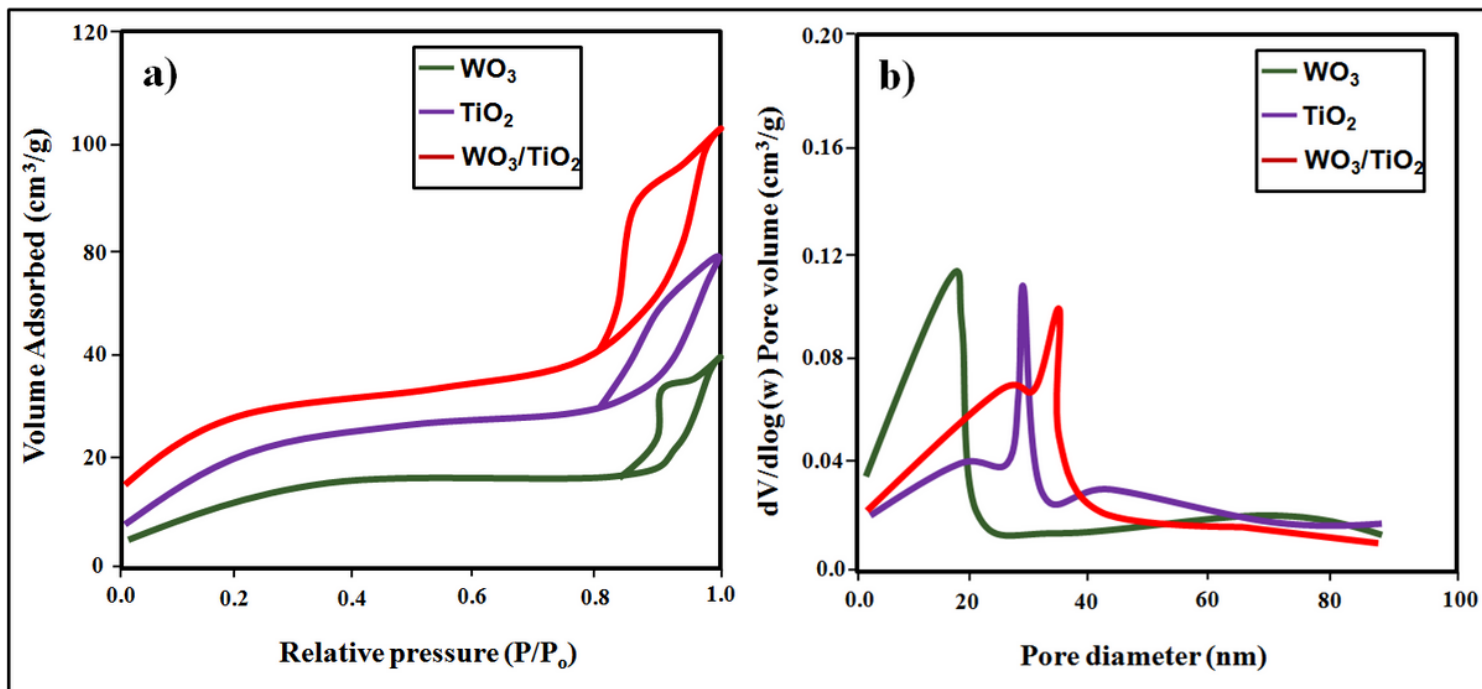


Figure 4

Raman spectra of the sensor films

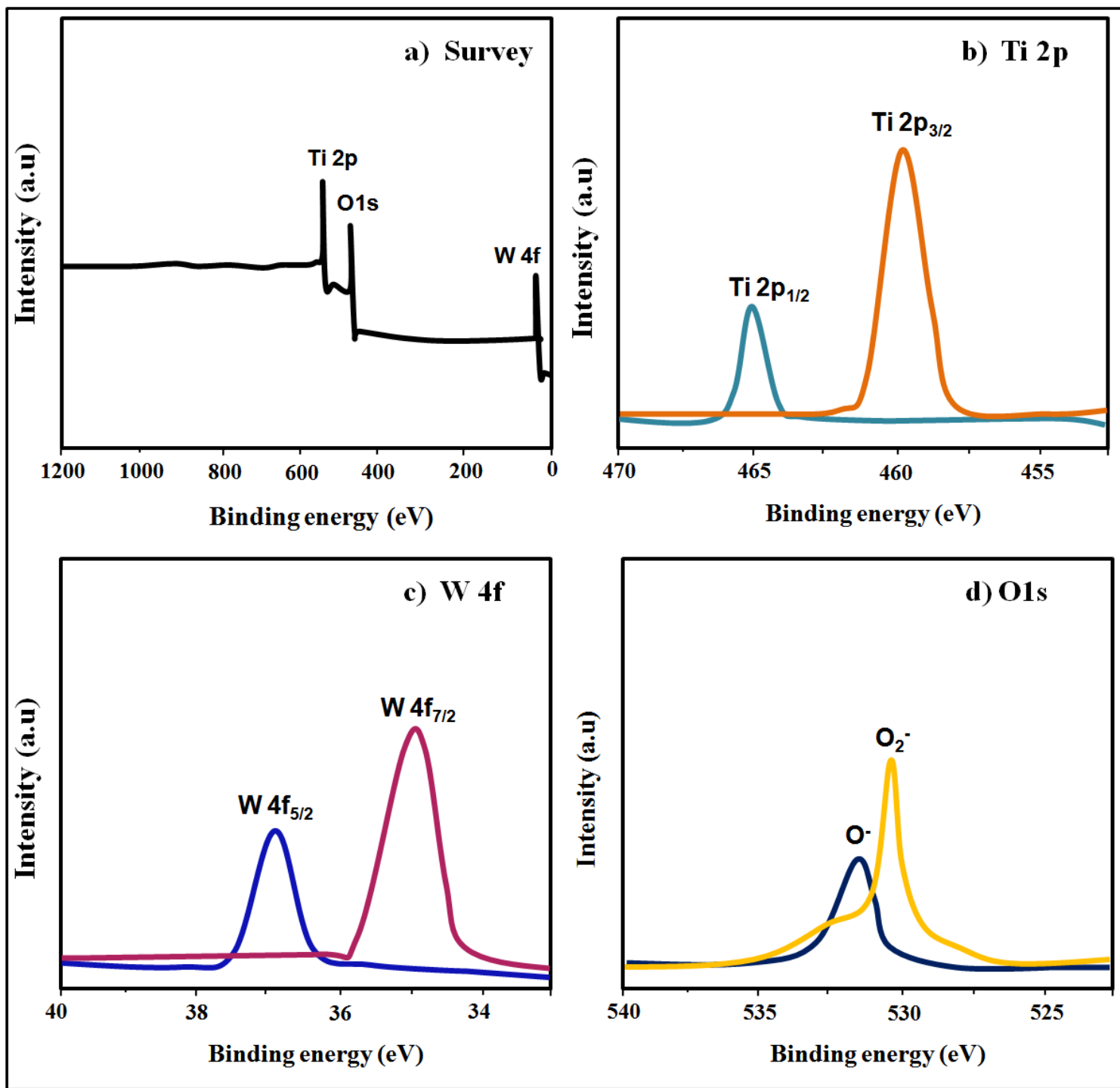


Figure 5

XPS spectra of WO₃/TiO₂ Hs (a) survey; (b) Ti 2p; (c) W 4f and (d) O 1s

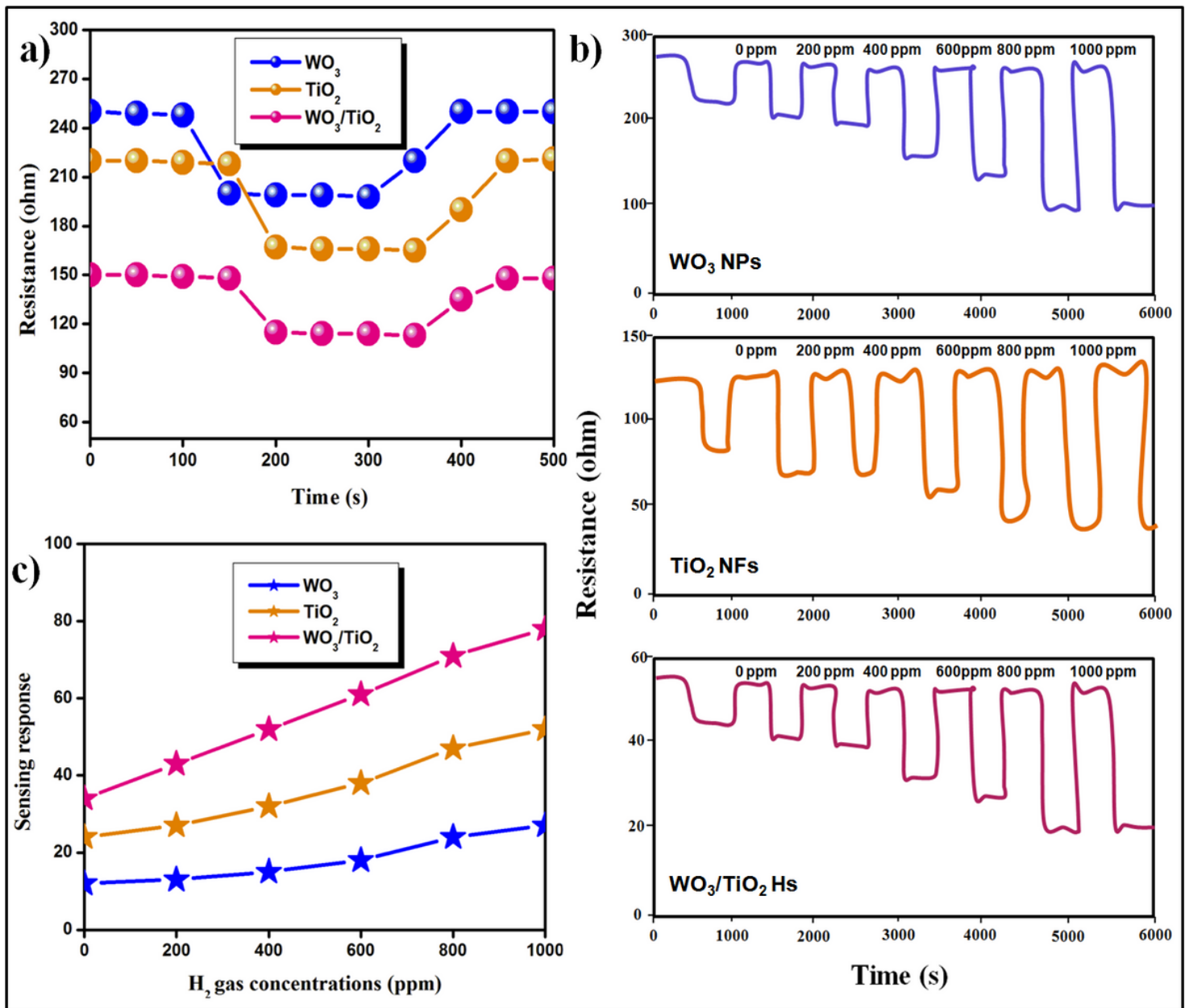


Figure 6

(a) Variation of resistance value of the sensors; Dynamic response of (b) WO₃ NPs, TiO₂ NFs, WO₃/TiO₂ Hs; c) Sensing response of H₂

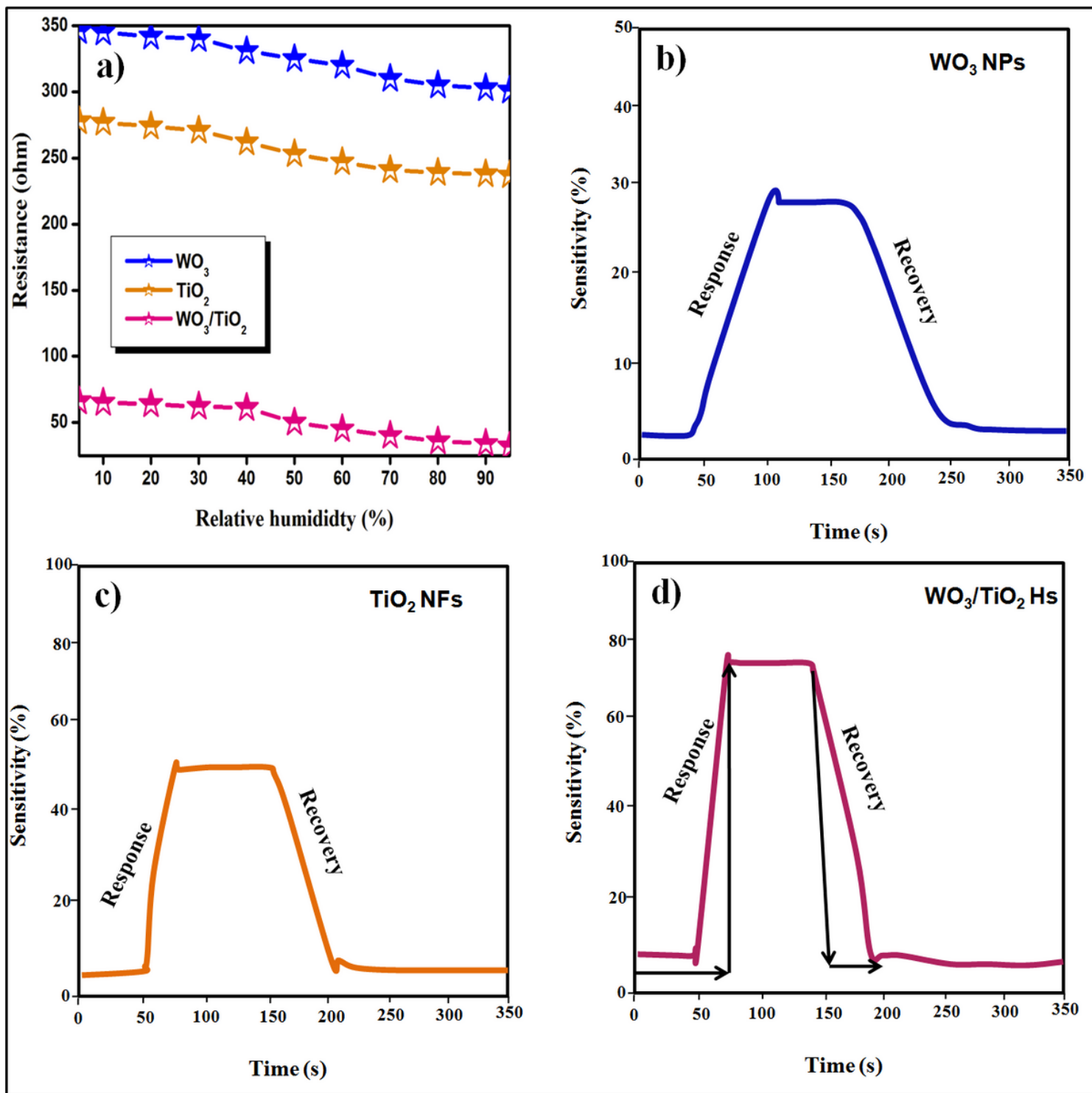


Figure 7

(a) Effect of humidity on the resistance of the sensors; Response and recovery time of the H₂ gas (b) WO₃ NPs; (c) TiO₂ NFs; (d) WO₃/TiO₂ Hs;

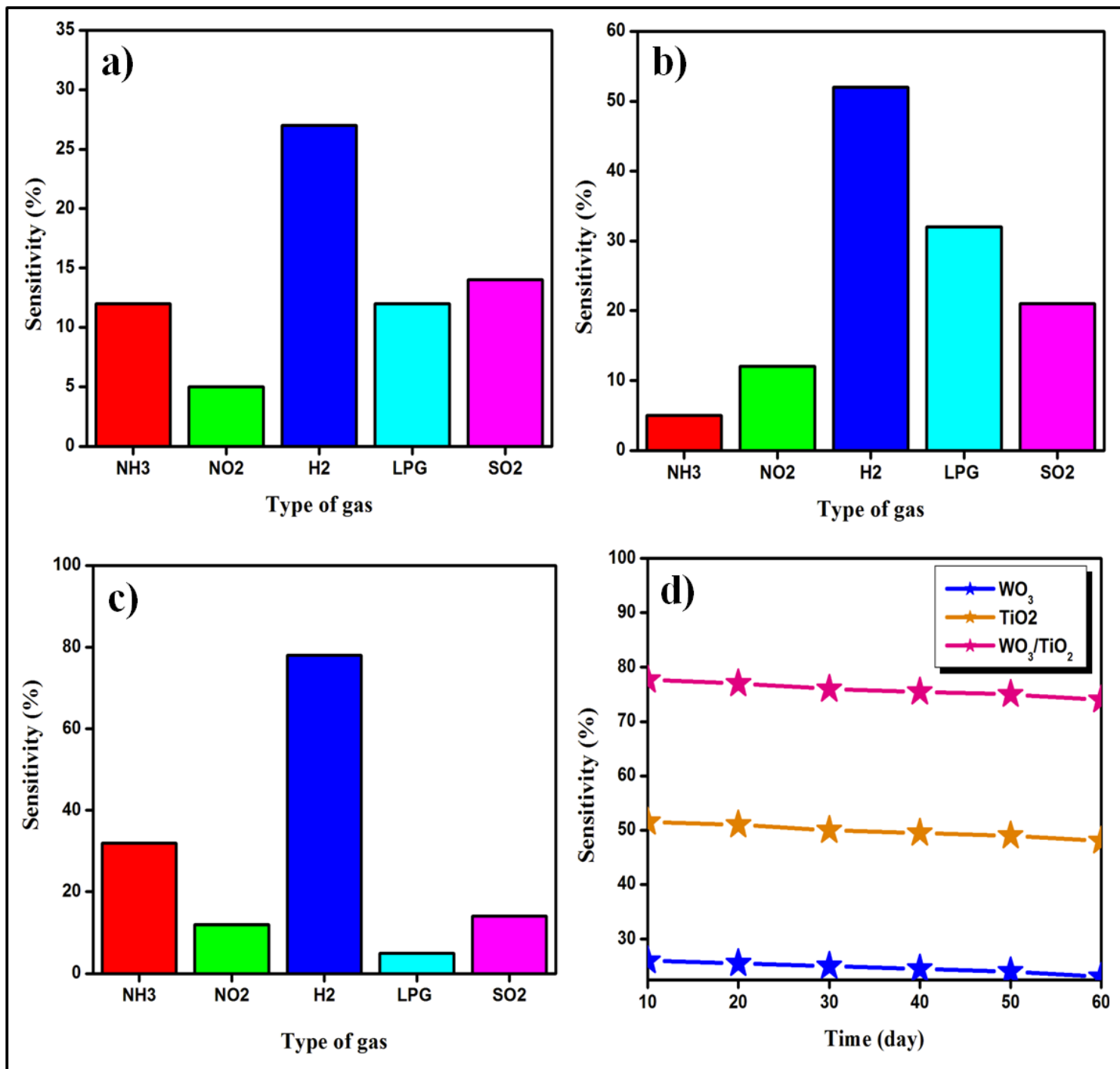


Figure 8

Selectivity gas sensing test of (a) WO₃ NPs; (b) TiO₂ NFs; (c) WO₃/TiO₂ Hs; (d) Stability test of all the sensor films

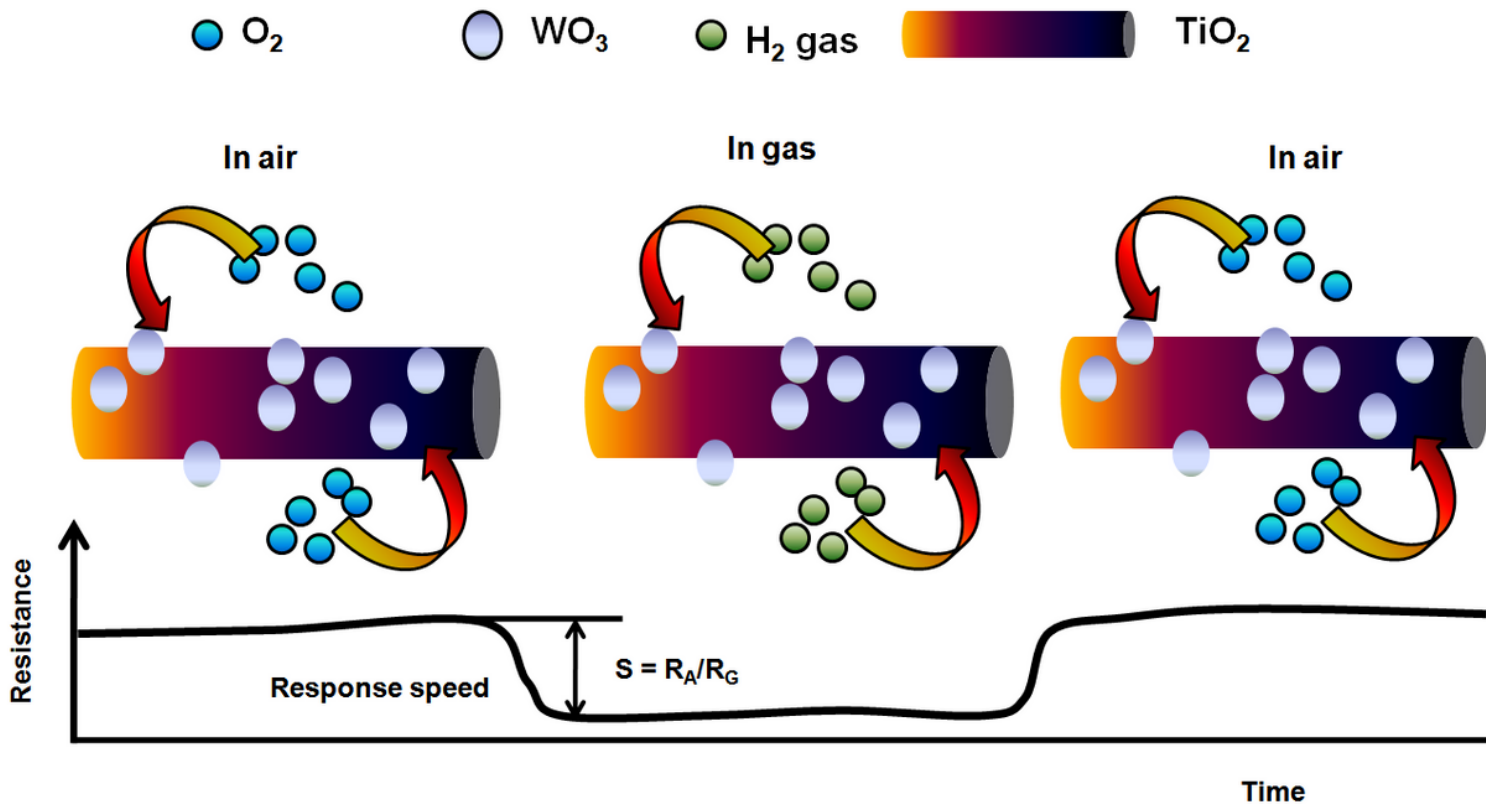


Figure 9

Gas sensing mechanism

Supplementary Files

This is a list of supplementary files associated with this preprint. Click to download.

- [Table1.doc](#)